Available online at www.sciencedirect.com
ScienceDirect
Ceramics International 37 (2011) 159–166
CERAMICS INTERNATIONAL
www.elsevier.com/locate/ceramint

Enhanced particle rearrangement during liquid phase spark plasma sintering of silicon nitride-based ceramics

Pilar Miranzo, Jesús González-Julián, María Isabel Osendi, Manuel Belmonte *

Institute of Ceramics and Glass (CSIC), Campus de Cantoblanco, Kelsen 5, 28049 Madrid, Spain

Received 15 December 2009; received in revised form 14 July 2010; accepted 29 July 2010
Available online 23 August 2010

Abstract

Densification evolution has been analysed in liquid phase assisted spark plasma sintering (SPS) of silicon nitride (Si_3N_4)-based materials. Monolithic ceramics with variable amounts of Al_2O_3/Y_2O_3 sintering additives, and carbon nanotubes (CNTs) containing Si_3N_4 composites have been considered. The shrinkage behaviour of SPSed monolithic Si_3N_4 showed a noticeable enhancement of the particle rearrangement stage, exhibiting a complete wetting of the grain boundary phase even for the lowest additive content (1.70 vol.%), unlike the corresponding hot pressed (HPed) material. An improvement of the liquid phase wetting by the presence of electromechanical forces is proposed to explain the enhanced densification occurring in the particle rearrangement stage of the SPS process. Furthermore, the addition of CNTs seems to increase the efficiency of this mechanism, decreasing the particle rearrangement temperature.

Keywords: A. Sintering; B. Microstructure-final; B. Nanocomposites; D. Si_3N_4

1. Introduction

The outstanding thermomechanical and tribological properties achieved with silicon nitride (Si_3N_4) ceramics during the last decades have promoted their use in different technological applications, such as engine components, ball bearings or metal cutting and shaping tools [1]. The densification of these materials is quite complex and commonly entails the use of sintering additives (generally a mixture of rare earth and metallic oxides) and temperatures above 1700 °C for promoting the liquid phase sintering (LPS) [2]. LPS mechanism includes particle rearrangement, solution-precipitation and Ostwald ripening grain growth stages that usually overlap. In this way, $\alpha \rightarrow \beta$-phase transformation and grain growth jointly occur in Si_3N_4 densification when conventional sintering (CS) techniques, such as pressureless sintering (PS), hot pressing (HP) or hot isostatic pressing (HIP), are employed. This complex sintering progression is advantageously used for tailoring microstructures and, hence, properties [3].

On the other hand, the spark plasma sintering (SPS) technique [4–6], a pressure assisted pulsed direct current sintering process, enhances the sinterability of Si_3N_4 leading to dense materials with negligible grain growth and phase transformation at reduced temperatures [7–10]. The phenomena responsible for the enhanced sintering are still under debate [5,11–16] and many efforts are presently focused on modelling the temperature and current profiles during SPS and also on analysing the microstructure evolution in different materials [15,17–20]. One of the first hypotheses was that a plasma generation between particles would cause the particle surface cleaning and mass transport improvement [14], but this proposal has been particularly controversial because the lack of experimental evidence of such a plasma formation [13]. Among the numerous SPS mechanisms proposed, a general consensus on the important role of both the Joule rapid heating [15] and the intrinsic field effects [4,15] exits. In the particular case of the LPSed Si_3N_4-based materials, Shen et al. [16] proposed a dynamic ripening mechanism to explain the very fast in situ formation of a tough interlocking microstructure. Then, this mechanism was mainly focused on the solution-precipitation stage of the LPS process, pointing to the enhanced motion of charged species caused by the electric field and rapid heating as responsible for the increased diffusion and homogenization in the liquid phase during this

* Corresponding author. Tel.: +34 91735586; fax: +34 917355843.
E-mail address: mbelmonte@icv.csic.es (M. Belmonte).

0272-8842/$36.00
doi:10.1016/j.ceramint.2010.08.019

stage. However, the dynamic ripening mechanism does not entirely explain the enhanced shrinkage observed during the first stages of sintering in Si_3N_4-based materials by SPS, where large densification without grain growth and with reduced phase transformation have been observed [7–10,21,22]. Therefore, some insight into the previous particle rearrangement stage is needed.

Here we focus on the effect that the pulsed electric field can have on the liquid phase distribution, thus affecting particle rearrangement. Two different Si_3N_4-based ceramics are considered: monolithic materials with different amounts of sintering additives and composites containing an electrically conductive second phase as carbon nanotubes (CNTs). The shrinkage rate, the microstructure and the morphological characteristics of each SPSed material are analysed. In the case of monolithics, results are compared with HP shrinkage data of similar materials. The improvement in the liquid phase wetting caused by the applied electric field is pointed out as the main responsible for the enhanced densification occurring during the initial densification stage of the SPS process.

2. Experimental procedure

For the Si_3N_4 monolithic materials, three different compositions (Table 1) containing α-Si_3N_4 (95% α-phase, SN-E10 grade, UBE Industries, Japan) and distinct amounts of aluminium oxide (Al_2O_3, grade SM8, Baikowski Chimie, France) and yttrium oxide (Y_2O_3, grade C, H. C. Starck GmbH & Co., Germany), as sintering additives, were attrition milled in ethanol for 2 h using Si_3N_4 grinding media. Afterwards, solvent was evaporated in a rotary-evaporator at 90 °C and the resultant mixture was oven dried at 120 °C before sieving through a 63 μm mesh. The different compositions were labelled as SN2A5Y, SN1A3Y and SN0.5A2Y (Table 1).

Regarding Si_3N_4 composites, multi-walled carbon nanotubes (MWCNTs, Nanolab Inc., MA, USA) in concentrations ranging from 1.8 to 8.6 vol.% were added to the SN2A5Y matrix powder, as described elsewhere [23]. In this case, the compositions were labelled as 1.8CNT, 5.3CNT and 8.6CNT (Table 1).

Disc shaped samples of 3 mm thickness and 20 mm diameter were SPSed (SPS-510CE, SPS Syntex Inc., Japan) using a heating rate of 133 °C min^{-1}, an uniaxial pressure of 50 MPa and a holding time of 5 min, under 4 Pa of vacuum atmosphere. In the monolithic materials the maximum sintering temperatures ranged from 1500 to 1675 °C, whereas in the composites it was set at 1585 °C to avoid nanotubes damage. For comparative purposes, some hot-press (HP, W150/200-2200-100, FCT Systeme GmbH, Germany) sintering runs of the monolithic compositions were done at temperatures of 1600–1750 °C, 10 °C min^{-1} of heating rate, an uniaxial pressure of 50 MPa, holding times of 5 and 90 min, under 0.1 MPa of N_2. HP technique was not used for the composites as it did not allow getting dense materials with undamaged nanotubes.

The sintering parameters for the complete set of monolithic materials (SPSed and HPed experiments) are summarized in Table 2. Temperature was controlled with a pyrometer that in the case of SPSed experiments was focused in a hole drilled through half the thickness of the die wall at half the height of the die. The SPS parameters, including voltage, current, temperature, vacuum level, axial pressure and total displacement (d_z), were computer recorded during the whole sintering process.

Apparent density of the specimens was determined by water immersion and/or helium pycnometry methods (Model MVP-1, Quanta Chrome Co., USA). Crystalline phases and α/β transformation degree were determined by X-ray diffraction (XRD, Bruker D5000, Siemens, Germany) procedures [24]. Microstructures of the specimens were observed using a field emission scanning electron microscope (FESEM, Hitachi S-4700, Japan) on polished and plasma etched (CF_4/5 vol.% O_2 at 100 W for 40 s) samples. Specimens containing MWCNTs were also prepared for observation in the transmission electron microscope (TEM, 200 kV JEOL JEM 2000 FX, Japan). Average Si_3N_4 grain diameter (d_{50}) and apparent aspect ratio (AR_{50}) were estimated on FESEM micrographs by image analysis techniques, measuring at least 1000 features.

3. Results and discussion

3.1. Monolithic ceramics

Density and α-phase content of each monolithic specimen are summarized in Table 2. For the composition with the highest amount of additives, SN2A5Y, SPS technique allowed attaining materials with a high density ($d_{rel} > 95\%$) and reduced phase transformation (76% α-phase) at temperatures as low as 1500 °C. The SN2A5Y material became fully dense, still retaining high α-phase contents (41%), at 1600 °C. Conversely, at this temperature, highly porous HPed specimens were

Table 1
Materials description: specimen label, powders composition in weight percentage (wt.%), sintering additives ratio, total volume percentage (vol.%) of sintering additives, and MWCNTs content in the composites (wt.% and vol.%).

Materials	Composition label	Si_3N_4 (wt.%)	Al_2O_3 (wt.%)	Y_2O_3 (wt.%)	Y_2O_3/Al_2O_3	Additives (vol.%)	MWCNTs (wt.%)	MWCNTs (vol.%)
Si_3N_4 monolithic ceramics	SN2A5Y	93.0	2.0	5.0	2.5	4.85	–	–
	SN1A3Y	96.0	1.0	3.0	3.0	2.74	–	–
	SN0.5A2Y	97.5	0.5	2.0	4.0	1.70	–	–
Si_3N_4 composites	1.8CNT	92.0	2.0	5.0	2.5	4.85	1.0	1.8
	5.3CNT	90.0	2.0	5.0	2.5	4.85	3.0	5.3
	8.6CNT	88.0	2.0	5.0	2.5	4.85	5.0	8.6

Table 2
Sintering parameters, densities and α-phase content for the SPSed and HPed monolithic materials. T and t are the maximum sintering temperature and the holding time, respectively; d and d_{rel} are the apparent and the relative densities.

Composition	Sintering	Sample ID	T (°C)	t (min)	d (g cm^{-3})	d_{rel} (%)	α-Phase (%)
SN2A5Y	SPS	SPS2A5Y-1500	1500	0	3.08	95.4	76
		SPS2A5Y-1600	1600	5	3.23	100.0	41
		SPS2A5Y-1650	1650	5	3.23	100.0	6
	HP	HP2A5Y-1600	1600	5	2.44	75.5	85
		HP2A5Y-1750	1750	90	3.23	100.0	0
SN1A3Y	SPS	SPS1A3Y-1600	1600	5	3.21	100.0	43
	HP	HP1A3Y-1750	1750	90	3.18	99.0	6
SN0.5A2Y	SPS	SPS0.5A2Y-1600	1600	5	2.96	92.8	39
		SPS0.5A2Y-1675	1675	5	3.19	100.0	15
	HP	HP0.5A2Y-1750	1750	90	3.12	97.8	13

obtained; actually it was necessary to increase the temperature and holding time up to 1750 °C and 90 min, respectively, to get fully dense HPed SN2A5Y samples, which also led to the complete α → β-phase transformation. When the amount of additives was reduced to 2.74 vol.% (SN1A3Y), similar results as SN2A5Y in terms of densification and α-phase content were found for the SPSed material at 1600 °C, whereas the HPed SN1A3Y showed some porosity (1%) and residual amount of α-phase (6%). Finally, the composition with the lowest additive content, SN0.5A2Y (1.7 vol.%), showed less sinterability requiring SPS temperatures of 1675 °C to get fully densification. In this case, HPed material had a d_{rel} of ∼98% at 1750 °C and higher temperatures would be required for complete densification.

Fig. 1 shows the SPS shrinkage curves for the 1600 °C runs of the three different additive compositions. The displacement, d_z, curves (Fig. 1a) evidence that shrinkage began at lower temperatures as the additive content increased, particularly for the SN2A5Y specimen, the sintering start temperature was approximately 100 °C below the start temperature in the other two compositions. The displacement rate, $d(d_z)/dt$, versus temperature curves for all the compositions (Fig. 1b) exhibited two peaks typically associated to the two steps of LPS, that is, the rearrangement of the Si_3N_4 particles (first maximum) and the solution-precipitation process (second maximum) [3]. The maximum shrinkage temperature shifted to lower values as the amount of additives increased, from 1342 °C for SN0.5A2Y to 1280 °C for SN2A5Y, showing a inverse linear dependence with the total additive content (Fig. 1c). Besides, the solution-precipitation peak also shifted to lower temperatures when increasing additives content. The shift is particularly notable for the SN2A5Y composition, maximum occurs at 1415 °C as opposite to 1576 °C for the SN0.5A2Y.

These differences in densification behaviour among compositions can be explained considering the distinct types of grain boundary phases. In this sense, the average composition of the grain boundary phase for each material was estimated from the present additive contents plus the SiO_2 covering the Si_3N_4 particles, which was calculated from the O_2 amount in the starting Si_3N_4 powders provided by the supplier (2 wt.%). For simplification reasons the presence of N element in the glassy phase was not considered. Those compositions were tentatively placed in the corresponding Y_2O_3–Al_2O_3–SiO_2 phase equilibrium diagram (Fig. 2) [25]. Despite the fact that the SN2A5Y grain boundary composition is located in a different compatibility triangle from that of SN1A3Y and SN0.5A2Y, all three have the same invariant point (Fig. 2) and, therefore, the onset of liquid phase formation should occur at the same temperature (<1400 °C). However, SN2A5Y will be completely melted at 1500 °C, whereas SN1A3Y and SN0.5A2Y will need higher temperatures (Fig. 2). This would explain the large shift of the shrinkage rate peaks towards lower temperatures for the SN2A5Y composition.

Petzow and Herrmann [3] studied the sintering behaviour of Si_3N_4 ceramics containing mixtures of Al_2O_3 plus Y_2O_3 ranging from 3.5 to 8.5 vol.%, using CS techniques. They observed similar peaks to the present case but at higher temperatures, ∼1320 and ∼1600 °C, respectively, being the solution-precipitation peak about four times more intense than that of the particle rearrangement stage. Considering the faster heating rates typical of SPS runs, compared to those of CS techniques, if same mechanisms had taken place, shrinkage phenomena in SPS would have occurred at higher temperatures in a narrower temperature span [26], but the opposite trend was observed (Fig. 1b). Comparing with Petzow's data [3], also plotted in Fig. 1b for similar Y_2O_3/Al_2O_3 additive ratio materials (2.0 [3] versus 2.5 for SN2A5Y specimen), it can be stated that densification accelerated for the SPS process in spite of the smaller volume of additives of present materials (4.9 vol.% versus 6.0 vol.% for Ref. [3]); that is, the rearrangement stage took place at slightly lower temperatures and, besides, a remarkable decrease (∼200 °C) in the temperature of the solution-precipitation stage was observed. Even more, the particle rearrangement was strengthened versus the solution-precipitation process in the SPS experiments, as the intensity ratio between the corresponding peaks, $I_{rearrangement}/I_{sol\text{-}prec}$, was twice (0.50) that of the CSed sample (0.25). This unusual enhancement of the rearrangement stage relative to the solution-precipitation stage must be attributed to the influence of an electric field.

Furthermore, experimental evidence of an improved wetting in the SPS process of Si_3N_4 materials was obtained through the microstructural observation of the SN0.5A2Y specimen (Fig. 3). This composition contained just 1.70 vol.% of additives and, according to the literature [27], their high Y_2O_3/Al_2O_3 ratio

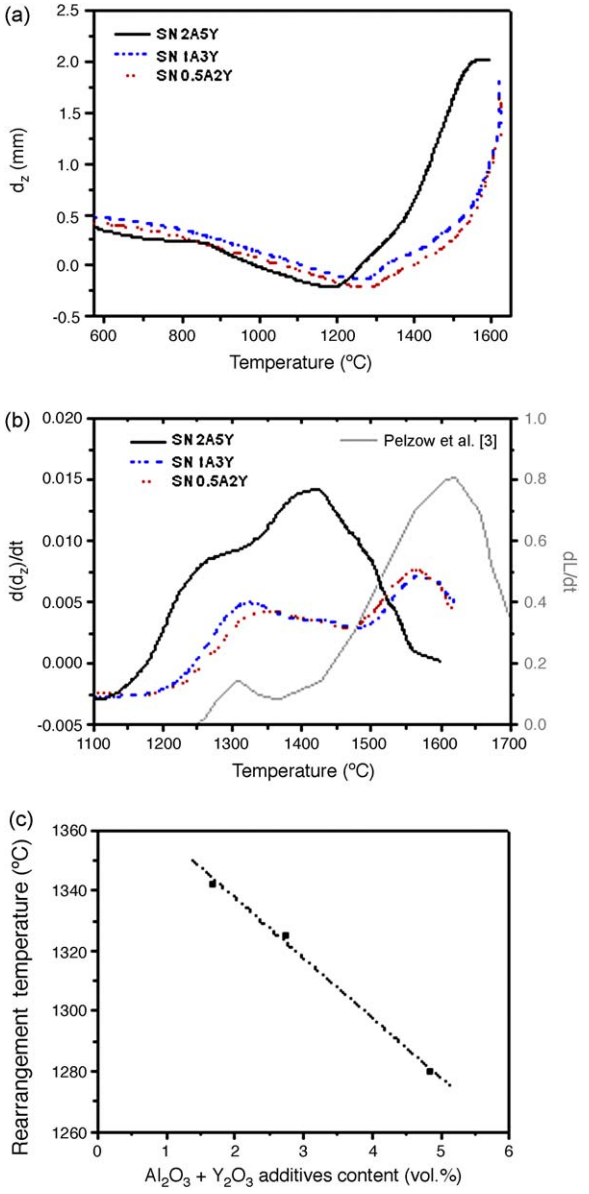

Fig. 1. Shrinkage behaviour of SPSed monolithic materials: (a) displacement (d_z) and (b) displacement rate (d(d_z)/dt) curves versus sintering temperature, (c) maximum temperature of the particle rearrangement stage as a function of the additives content. Petzow's data re-plotted from Ref. [3] for conventionally sintered Si_3N_4 with 6.0 vol.% of additives in a 2:1 weight ratio (Y_2O_3:Al_2O_3) are also included in (b).

should lead to a poor liquid wettability. This was confirmed in the corresponding HPed specimen as large pockets of glassy phase were observed across the specimen (Fig. 3a and b). However, the SPSed sample (Fig. 3c and d) showed a well distributed grain boundary glassy phase surrounding the Si_3N_4 grains in the whole material, supporting the statement that the electric field affects the liquid wetting.

Similarly as electromigration has been considered as the main effect in SPS of solid particles, the electromechanical forces acting on liquids should be correspondingly considered in the liquid phase SPS process. These forces are interface related phenomena and typically act when dielectric or aqueous liquids are in contact with an electrode or a dielectric film and a

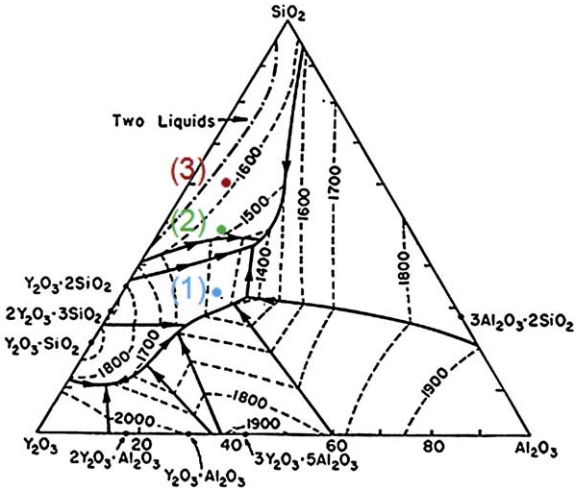

Fig. 2. Y_2O_3–Al_2O_3–SiO_2 phase equilibrium diagram [25] (in wt.%) showing the location of the SN2A5Y (1), SN1A3Y (2), and SN0.5A2Y (3) grain boundary compositions.

voltage (ac or dc) is applied to the system. Experimentally, these forces manifest by a reduction of the liquid contact angle and by the height-of rise effect [28,29], both phenomena being dependent of the squared applied voltage, V^2. Then, as particle rearrangement is governed by capillary forces acting on the liquid phase at grain junctions and the shrinkage rate increases as the contact angle decreases, a strong effect of the electromechanical forces on the initial step of LPS can be predicted, which would explain the enhanced sintering rate observed in SPSed Si_3N_4 during the first sintering stage.

Fig. 4 shows the scheme of a classical electrowetting on dielectric (EWOD) device. In the SPS set up, the voltage is supplied through the carbon die, Si_3N_4 grains would act as dielectric layers and the liquid would be the grain boundary liquid phase formed at high temperature. In this way, the voltage applied on sintering would reduce the solid–liquid interfacial tension, lowering contact angle and increasing capillary forces at contacts between particles [28–30]. As the voltage applied in SPS tests is rather low (∼5 V), the main limitation to the proposed model would be the high voltages (>100 V) experimentally reported [28] for significant contact angle reduction in electrolyte droplets over a dielectric layer. However, two important circumstances should not be missed, the low Si_3N_4 particle size and the high sintering temperatures. Regarding the first one, recent studies state that the above phenomena can take place at voltages as low as 6–15 V [31–33] for high dielectric constant materials if the thickness of the dielectric layer decreases down to 20–70 nm.

On the other hand, the reduction in the contact angle from θ_0, where there is not applied voltage, to θ when a voltage V is applied is given by the following expressions [28], depending on the system configuration:

$$\cos\theta = \cos\theta_0 + \frac{\varepsilon_l \cdot \varepsilon_0}{2 \cdot d_{EDL} \cdot \gamma_{lv}} V^2 \quad (1)$$

for liquid wetting on the metallic electrode, where ε_l is the dielectric constant of the liquid, ε_0 the vacuum permittivity, γ_{lv}

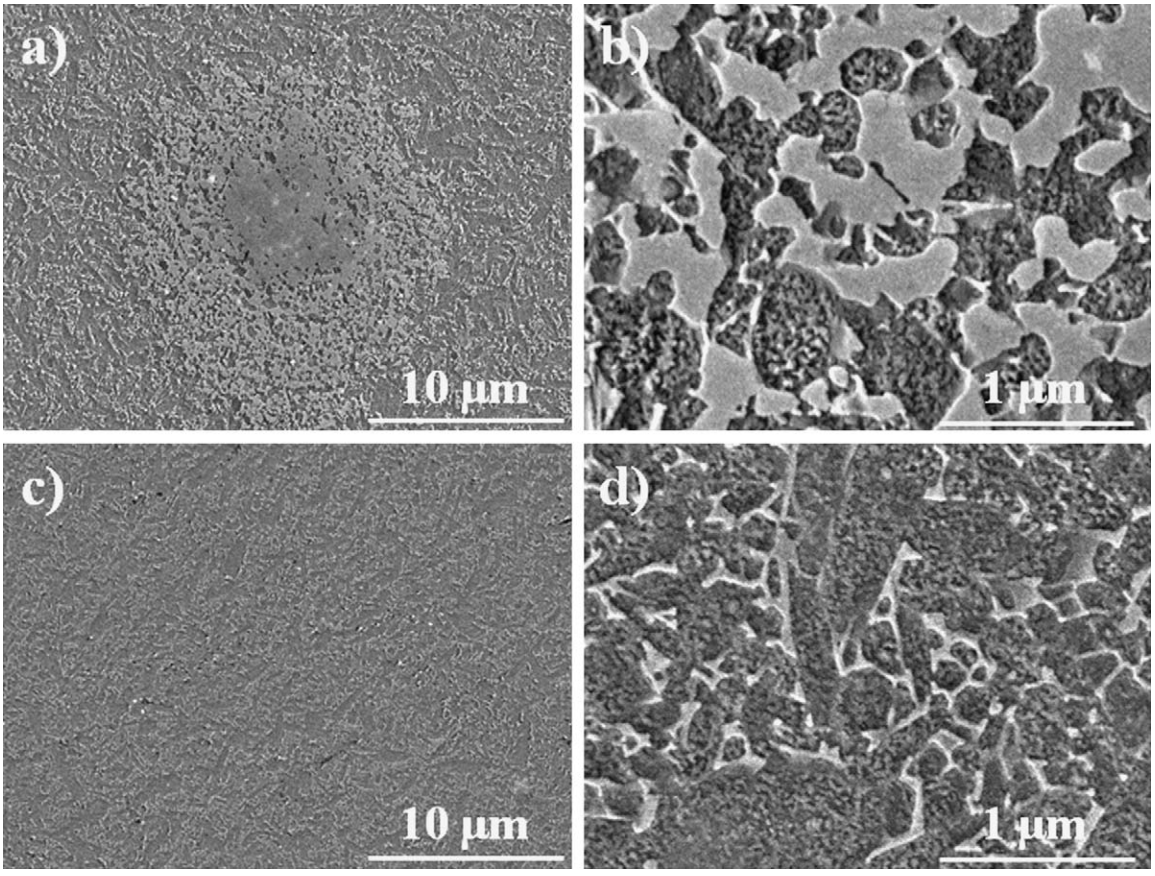

Fig. 3. FESEM micrographs of the polished and etched surfaces corresponding to HP0.5A2Y-1750 (a and b) and SPS0.5A2Y-1675 specimens (c and d), showing the different grain boundary glassy phase distributions at two magnifications. Light grey areas correspond to the intergranular glassy phase.

the liquid/vapour surface energy per unit area and d_{EDL} is the thickness of the electric double layer;

$$\cos\theta = \cos\theta_0 + \frac{\varepsilon_d \cdot \varepsilon_0}{2 \cdot d \cdot \gamma_{lv}} V^2 \quad (2)$$

for liquid wetting on a dielectric layer (EWOD model). In this equation, ε_d is the dielectric constant of the dielectric layer and d is its thickness. Main differences between both systems are related to the thickness of the involved layer. In the case of the electric conductor, Eq. (1), that is the electric double layer formed at the contact surface, which is 1–10 nm in thickness; whereas, for the EWOD configuration, Eq. (2), it is the thickness of the dielectric layer that is in the micrometer range. This means that the voltage required for the same contact angle reduction is $\sqrt{d/d_{EDL}} = 10 - 10^{3/2}$ times higher in the EWOD than in the classical electrowetting mechanism. Therefore, the high voltages (>100 V) reported for a significant reduction in contact angle in EWOD could go down to values as low as 3 V if the substrate is an electrical conductor. This represents the base for understanding the proposed crucial role of the temperature. Ceramics are generally good dielectric materials whose electric conductivity increases with temperature. Electrons, generally trapped in localized states, can move through an insulator because of random thermal fluctuations will give that electron enough energy to get out of its localized state, and move to the conduction band. Once there, the electron can move through the crystal before relaxing into another localized state. Additionally, in the presence of an electric field, the electron does not need as large thermal fluctuation and it will be able to jump more frequently by the Frenkel–Poole effect [34]:

$$J \propto E \cdot \exp\left(\frac{-q \cdot (\phi_B - \sqrt{qE/\pi\varepsilon})}{k_B \cdot T}\right) \quad (3)$$

where J is the current density, E the applied electric field, q the elementary charge, ϕ_B the voltage barrier (in zero applied electric field) that an electron must cross to move from one atom to another in the crystal, ε is dynamic permittivity, k_B is Boltzmann's constant and T is the temperature. Assuming that there is not applied electric field, a simple calculation can be made to compare the current density at the SPS temperature, J_T,

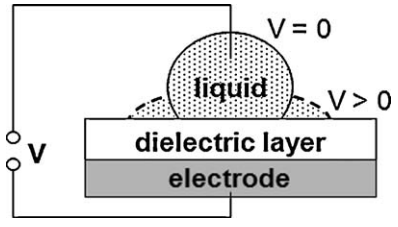

Fig. 4. Scheme of the electrowetting on dielectric device.

with the current density at room temperature, J_{RT}:

$$\frac{J_T}{J_{RT}} \propto \exp\left(\frac{-q \cdot \phi_B}{k_B}\left(\frac{1}{T} - \frac{1}{RT}\right)\right) \approx 10^{70} \quad (4)$$

where T and RT are the SPS and room temperatures, respectively, and an energy barrier for Si_3N_4 of 5 eV, independent of the temperature, has been introduced [35]. Therefore, due to the high sintering temperatures (above 1500 °C) and the presence of an electric field in the SPS tests, contact angle reduction in SPS of Si_3N_4 would be better modelled by Eq. (1) than by the EWOD equation (Eq. (2)), and significant changes in wetting could be expected in spite of the low voltages involved in SPS.

Besides the described electromechanical forces acting on the liquid phase, the dynamic ripening mechanism [16] can account for the enhanced sintering also observed in the solution-precipitation stage (Fig. 1b). This phenomenon is identified in Fig. 5 for SN2A5Y specimens as microstructure evolves from sub-micron equiaxed grains with negligible grain growth (average particle size, d_{50}, of 190 nm and aspect ratio, AR_{50}, of 1.4) at 1500 °C, towards coarser bimodal microstructures at 1600 and 1650 °C (d_{50} = 300 and 570 nm, AR_{50} = 1.8 and 2.4, respectively), in correspondence with a significant decrease in the α-phase content from 76% at 1500 °C to 6% at 1650 °C (Table 2).

3.2. Si_3N_4/MWCNTs composites

The shrinkage behaviour of the SN2A5Y matrix is strongly modified by adding MWCNTs (Fig. 6). In this way, the peak temperature linked to the particle rearrangement stage decreased from 1280 to 1220 °C (Fig. 6b) with just 1.8 vol.% of MWCNTs (1.8CNT). That temperature progressively increased, following a second order polynomial fitting, with the amount of nanotubes, although it never exceeded that of the monolithic material. Conversely, the temperature of the

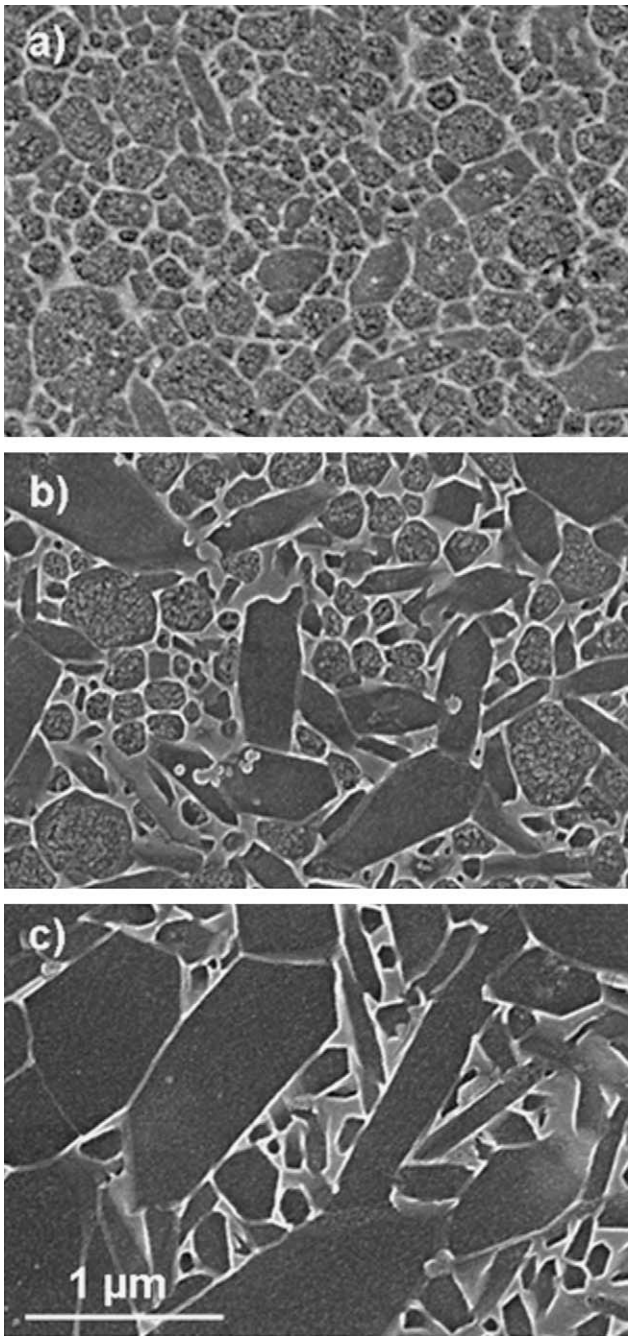

Fig. 5. FESEM micrographs of the polished and etched surfaces corresponding to SPSed SN2A5Y materials as a function of the sintering temperature: (a) SPS2A5Y-1500, (b) SPS2A5Y-1600 and (c) SPS2A5Y-1650.

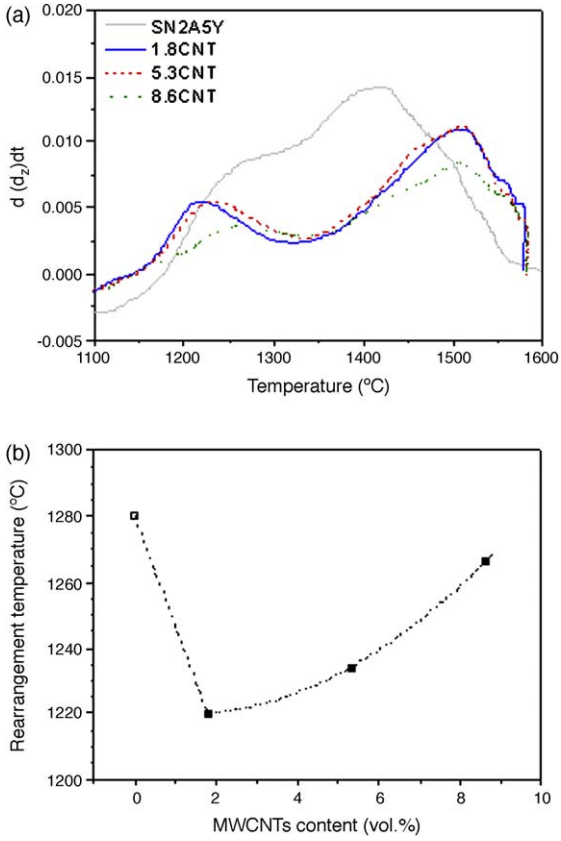

Fig. 6. Shrinkage behaviour of SPSed composites: (a) displacement rate (d(d_z)/dt) curves versus sintering temperature and (b) maximum temperature of the particle rearrangement stage as a function of the MWCNTs content.

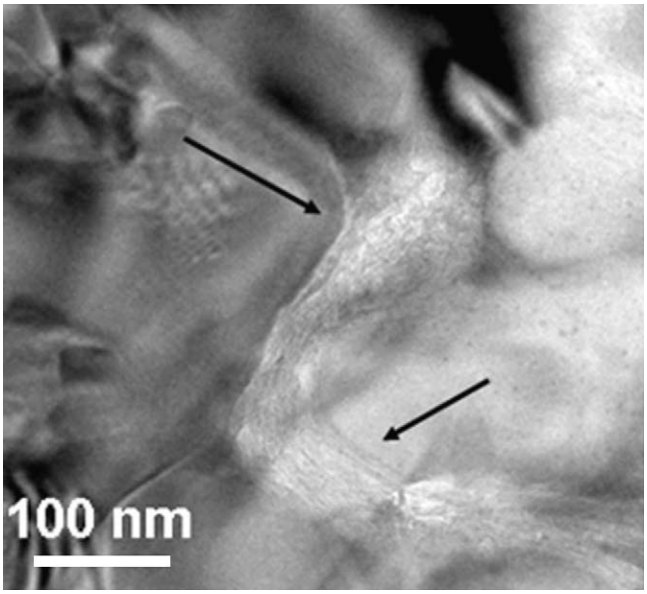

Fig. 7. TEM micrograph for the composite containing 5.3 vol.% of MWCNTs. The nanotubes are pointed out by arrows.

solution-precipitation stage for the composites shifted ~100 °C towards higher values compared to the monolithic material. The intensity ratio between particle rearrangement and solution-precipitation peaks was around 0.5 for all the composites, similarly to the monolithic materials, which again evidences the increased weight of particle rearrangement in the sintering process, explained by the effect of the electric field on the liquid as well.

On the other hand, as it has been previously reported by the present authors [10,36], the electrical conductivity of the composites increased more than ten orders of magnitude with small additions of MWCNTs, changing from typically insulator Si_3N_4 to a semiconductor material, at room temperature. As the MWCNTs were located around the Si_3N_4 grains (Fig. 7), they would act as effective local conductive electrodes, enhancing the effectiveness of the electromechanical forces. Consequently, particle rearrangement should be improved justifying that it took place at lower temperatures compared to the monolithic material (Fig. 6b). However, this effect must compete with the well known retardation of densification associated to the development of tensile stresses in composites that contain non-sinterable particles of high aspect ratio [37,38]. This competition would explain the progressive increase in the particle rearrangement temperature with the MWCNTs content. Similarly, the MWCNTs networks would hinder the densification as sintering progresses, shifting the solution-precipitation maxima towards higher temperatures and refining the matrix grain size due to the incomplete development of that stage. In fact, the microstructural analysis of the composites with similar α-phase content (~40%) revealed that the addition of MWCNTs decreased d_{50} and AR_{50} from 297 to 233 nm (22%) and from 1.79 to 1.56 (13%) for SN2A5Y and 8.6CNT materials, respectively, as seen in Fig. 8.

It could be argued that MWCNTs additions introduce some impurities, which may decrease the melting temperature of the liquid phase. Nevertheless, this would not explain by itself the observed phenomenon as the nanotubes contain just ~1 wt.% of impurities, mainly iron (0.94 wt.%), and the rearrangement temperature increases with the MWCNTs additions.

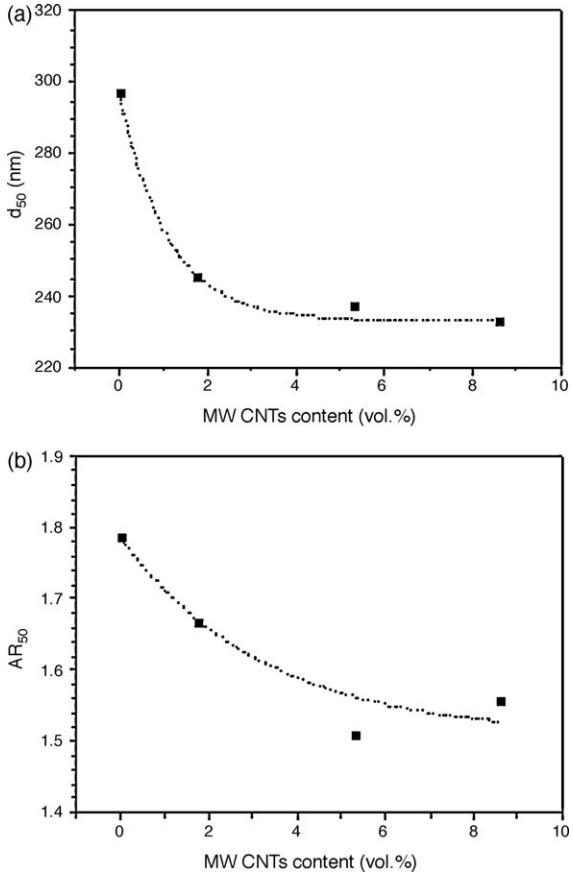

Fig. 8. (a) Average Si_3N_4 grain diameter (d_{50}) and (b) apparent aspect ratio (AR_{50}) for the composites as a function of the MWCNTs content. The α-phase content for all the specimens was ~40%.

4. Conclusions

The sintering kinetic and the homogenization of the liquid phase in Si_3N_4-based materials extraordinarily increase when the SPS technique is employed. The displacement rate curves of SPSed monolithic materials show a noticeable enhancement of the particle rearrangement stage compared to conventional sintering data. Furthermore, experiments conducted by SPS and HP in Si_3N_4 with very low additive content reveal large glassy pockets in the case of the HPed material, in contrast to the complete grain boundary phase wetting of the SPSed specimen.

An improvement of the liquid phase wetting and the capillary forces by the presence of an electric field is proposed to explain the enhanced densification occurring in the particle rearrangement stage of the liquid phase SPS process.

Small additions of an electrically conductive phase as carbon nanotubes increase the effectiveness of the proposed mechanism, leading to a decrease in the particle rearrangement temperature compared to the monolithic materials. However,

the interconnected MWCNTs retard the densification in the further stages and refine the matrix grain size.

Acknowledgements

The financial support of Spanish Ministry of Science and Innovation through projects MAT2006-7118, MAT2009-09600 and HA2007-0083 is recognized. J. Gonzalez-Julian acknowledges the financial support of the JAE (CSIC) fellowship Program.

References

[1] F.L. Riley, Silicon nitride and related materials, J. Am. Ceram. Soc. 83 (2) (2000) 245–265.
[2] D. Suttor, G.S. Fischman, Densification and sintering kinetics in sintered silicon nitride, J. Am. Ceram. Soc. 75 (5) (1992) 1063–1067.
[3] G. Petzow, M. Herrmann, Silicon nitride ceramics, Struct. Bond. 102 (2002) 47–167.
[4] M. Tokita, Mechanism of spark plasma sintering and its application to ceramics, Nyu Seramikkusu 10 (1997) 43–53.
[5] Z.A. Munir, U. Anselmi-Tamburini, M. Ohyanagi, The effect of electric field and pressure on the synthesis and consolidation of materials: a review of the spark plasma sintering method, J. Mater. Sci. 41 (3) (2006) 763–777.
[6] R. Orru, R. Licheri, A.M. Locci, A. Cincotti, G. Cao, Consolidation/synthesis of materials by electric current activated/assisted sintering, Mater. Sci. Eng. R 63 (4–6) (2009) 127–287.
[7] T. Nishimura, M. Mitomo, H. Hirotsuru, M. Kawahara, Fabrication of silicon-nitride nano-ceramics by spark plasma sintering, J. Mater. Sci. Lett. 14 (15) (1995) 1046–1047.
[8] M. Suganuma, Y. Kitagawa, S. Wada, N. Murayama, Pulsed electric current sintering of silicon nitride, J. Am. Ceram. Soc. 86 (3) (2003) 387–394.
[9] Z. Shen, H. Peng, J. Liu, M. Nygren, Conversion from nano- to micron-sized structures: experimental observations, J. Eur. Ceram. Soc. 24 (12) (2004) 3447–3452.
[10] M. Belmonte, J. Gonzalez-Julian, P. Miranzo, M.I. Osendi, Spark plasma sintering: a powerful tool to develop new silicon nitride-based materials, J. Eur. Ceram. Soc. 30 (4) (2010) 2937–2946.
[11] E.A. Olevsky, S. Kandukuri, L. Froyen, Consolidation enhancement in spark-plasma sintering: impact of high heating rates, J. Appl. Phys. 102 (11) (2007) 114913.
[12] R. Chaim, Densification mechanisms in spark plasma sintering of nanocrystalline ceramics, Mater. Sci. Eng. A 443 (1–2) (2007) 25–32.
[13] D.M. Hulbert, A. Anders, D.V. Dudina, J. Andersson, D. Jiang, C. Unuvar, U. Anselmi-Tamburini, E.J. Lavernia, A.K. Mukherjee, The absence of plasma in spark plasma sintering, J. Appl. Phys. 104 (3) (2008) 033305.
[14] J.R. Groza, M. Garcia, J.A. Schneider, Surface effects in field-assisted sintering, J. Mater. Res. 16 (1) (2001) 286–292.
[15] U. Anselmi-Tamburini, S. Gennari, J.E. Garay, Z.A. Munir, Fundamental investigations on the spark plasma sintering/synthesis process: II. Modeling of current and temperature distributions, Mater. Sci. Eng. A 394 (1–2) (2005) 139–148.
[16] Z.J. Shen, Z. Zhao, H. Peng, M. Nygren, Formation of tough interlocking microstructures in silicon nitride ceramics by dynamic ripening, Nature 417 (6886) (2002) 266–269.
[17] K. Vanmeensel, A. Laptev, J. Hennicke, J. Vleugels, O. Van der Biest, Modelling of the temperature distribution during field assisted sintering, Acta Mater. 53 (16) (2005) 4379–4388.
[18] G. Maizza, S. Grasso, Y. Sakka, T. Noda, O. Ohashi, Relation between microstructure, properties and spark plasma sintering (SPS) parameters of pure ultrafine WC powder, Sci. Technol. Adv. Mater. 8 (7–8) (2007) 644–654.
[19] D. Tiwari, B. Basu, K. Biswas, Simulation of thermal and electric field evolution during spark plasma sintering, Ceram. Int. 35 (2) (2009) 699–708.
[20] J. Räthel, M. Herrmann, W. Beckert, Temperature distribution for electrically conductive and non-conductive materials during field assisted sintering (FAST), J. Eur. Ceram. Soc. 29 (8) (2009) 1419–1425.
[21] G.H. Peng, M. Liang, Z.H. Liang, Q.Y. Li., W.L. Li, Q.Q. Liu, Spark plasma sintering silicon nitride ceramics with high thermal conductivity using $MgSiN_2$ as additives, J. Am. Ceram. Soc. 92 (9) (2009) 2122–2124.
[22] M. Belmonte, A. de Pablos, P. Miranzo, M.I. Osendi, Spark plasma sintering of Si_3N_4-based materials, in: Y. Grin, B. Kieback, J. Schmidt (Eds.), Proceedings of Advanced Processing for Novel Functional Materials, Max-Plank-Institut für Chemische Physik fester Stoffe, Dresden, 2009, pp. 41–46.
[23] M.I. Osendi, F. Gautheron, P. Miranzo, M. Belmonte, Dense and homogenous silicon nitride composites containing carbon nanotubes, J. Nanosci. Nanotechnol. 9 (10) (2009) 6188–6194.
[24] C.P. Gazzara, D.R. Messier, Determination of phase content of Si_3N_4 by X-ray-diffraction analysis, Am. Ceram. Soc. Bull. 56 (9) (1997) 777–780.
[25] I.A. Bondar, F.Ya. Galakhov, Phase equilibria in the system Y_2O_3–Al_2O_3–SiO_2, Izv. Akad. Nauk SSSR, Ser. Khim. 7 (1963) 1325.
[26] O. Abe, Sintering process of Y_2O_3 and Al_2O_3-doped Si_3N_4, J. Mater. Sci. 25 (9) (1990) 4018–4026.
[27] H. Lemercier, T. Rouxel, D. Fargeot, J.L. Besson, B. Piriou, Yttrium SiAlON glasses: structure and mechanical properties—elasticity and viscosity, J. Non-Cryst. Solids 201 (1–2) (1996) 128–145.
[28] F. Mugele, J.C. Baret, Electrowetting: from basics to applications, J. Phys. Condes. Matter. 17 (28) (2005) R705–R774.
[29] T.B. Jones, K.L. Wang, D.J. Yao, Frequency-dependent electromechanics of aqueous liquids: electrowetting and dielectrophoresis, Langmuir 20 (7) (2004) 2813–2818.
[30] M.W.J. Prins, W.J.J. Welters, J.W. Weekamp, Fluid control in multichannel structures by electrocapillary pressure, Science 291 (5502) (2001) 277–280.
[31] H. Moon, S.K. Cho, R.L. Garrell, C.J. Kim, Low voltage electrowetting-on-dielectric, J. Appl. Phys. 92 (7) (2002) 4080–4087.
[32] Y. Li, W. Parkes, L.I. Haworth, A.W.S. Ross, J.T.M. Stevenson, A.J. Walton, Room-temperature fabrication of anodic tantalum pentoxide for low-voltage electrowetting on dielectric (EWOD), J. Microelectromech. Syst. 17 (6) (2008) 1481–1488.
[33] J.H. Chang, D.Y. Choi, S. Han, J.J. Pak, Driving characteristics of the electrowetting-on-dielectric device using atomic-layer-deposited aluminium oxide as the dielectric, Microfluid. Nanofluid. 8 (2) (2010) 269–273.
[34] S.M. Sze, K.K. Ng, Physics of Semiconductor Devices, 3rd ed., Wiley-Interscience, by John Wiley and Sons, Inc. Section 4.3.4, Hoboken, NJ, USA, 2007.
[35] Y.N. Xu, W.Y. Ching, Electronic structure and optical properties of α and β phases of silicon nitride, silicon oxynitride, and with comparison to silicon dioxide, Phys. Rev. B 51 (24) (1995) 17379–17389.
[36] J. Gonzalez-Julian, Y. Iglesias, A.C. Caballero, M. Belmonte, P. Miranzo, M.I. Osendi, Multi-scale electrical response of silicon nitride/multi-walled carbon nanotubes composites, Comp. Sci. Technol. (submitted for publication).
[37] O. Sudre, F.F. Lange, Effect of inclusions on densification: I, Microstructural development in an Al_2O_3 matrix containing a high-volume fraction of ZrO_2 inclusions, J. Am. Ceram. Soc. 75 (3) (1992) 519–524.
[38] M. Belmonte, J.S. Moya, P. Miranzo, Bimodal sintering of Al_2O_3/Al_2O_3 platelet ceramic composites, J. Am. Ceram. Soc. 78 (6) (1995) 1661–1667.